Japanese Journal of Applied Physics

REGULAR PAPERS

Bismuth doping effect on crystal structure and photodegradation activity of Bi–TiO_2 nanoparticles

To cite this article: Ming-Chung Wu *et al* 2017 *Jpn. J. Appl. Phys.* **56** 04CJ01

Japanese Journal of Applied Physics **56**, 04CJ01 (2017)
https://doi.org/10.7567/JJAP.56.04CJ01

REGULAR PAPER

Bismuth doping effect on crystal structure and photodegradation activity of Bi–TiO_2 nanoparticles

Ming-Chung Wu[1,2,3]*, Yin-Hsuan Chang[1], and Ting-Han Lin[1]

[1]*Department of Chemical and Materials Engineering, College of Engineering, Chang Gung University, Taoyuan 33302, Taiwan*
[2]*Center for Reliability Sciences and Technologies, Chang Gung University, Taoyuan 33302, Taiwan*
[3]*Division of Neonatology, Department of Pediatrics, Chang Gung Memorial Hospital, Taoyuan 33305, Taiwan*

*E-mail: mingchungwu@mail.cgu.edu.tw

Received October 12, 2016; accepted November 20, 2016; published online January 17, 2017

The bismuth precursor is adopted as dopant to synthesize bismuth doped titanium dioxide nanoparticles (Bi–TiO_2 NPs) with sol–gel method following by the thermal annealing treatment. We systematically developed a series of Bi–TiO_2 NPs at several calcination temperatures and discovered the corresponding crystal structure by varying the bismuth doping concentration. At a certain 650 °C calcination temperature, the crystal structure of bismuth titanate ($Bi_2Ti_2O_7$) is formed when the bismuth doping concentration is as high as 10.0 mol %. The photocatalytic activity of Bi–TiO_2 NPs is increased by varying the doping concentration at the particular calcination temperature. By the definition X-ray diffraction (XRD) structural identification, a phase diagram of Bi–TiO_2 NPs in doping concentration versus calcination temperature is provided. It can be useful for further study in the crystal structure engineering and the development of photocatalyst.

1. Introduction

Photocatalysts have raised a lot of interests to study due to the contribution to organic pollutant decomposition and the renewable energy production.[1–4] Among various photocatalysts, TiO_2 is widely used because of its giant advantages, such as environmentally friendly, chemical and thermal stability, low cost, highly active photocatalytic property and non-toxic to human.[5–9] TiO_2 also can be used in photovoltaic device electrode, photocatalytic hydrogen production and environmental pollution management.[10–16] Three kinds of TiO_2 crystal structures are formed in nature, including anatase, rutile and brookite.[17,18] Anatase and rutile are the most common crystal structures in TiO_2 presented in tetragonal arrangement, and they are often used to prepare high performance photocatalyst. It is a n-type semiconductor material with wide bandgap. However, its wide band gap (anatase ~3.2 eV; rutile ~3.0 eV) is located at ultraviolet light irradiation.[19,20] There is a practical application gap if the fine material/device of TiO_2 is usually exposed under sun light. Thus, the doping of metal ions into TiO_2 has been studied to enhance the absorption ability over the visible light spectrum.[21–24]

In recent years, Bi–TiO_2 material has been applied in many applications. The fabricated all-oxide solid-state dye-sensitized solar cells (DSSCs) with Bi–TiO_2 nanorods reveals high power conversion efficiency due to the high dye loading, slower charge recombination rate and the high electrical conductivity.[25] Bi–TiO_2 nanofibers is applied as the scattering layer of DSSCs, and it can enhance the open-circuit voltage successfully.[26] Bi–TiO_2 nanofibers fabricated by the hydrothermal method exhibits an enhancement for the photodegradation of organic dye and the photocatalytic hydrogen generation.[24] Doping bismuth ion into TiO_2 nanoparticles prepared by sol–gel method can narrow the bandgap of TiO_2 and improve the CO_2 adsorption ability.[27] Furthermore, Bi–TiO_2 can enhance ethanol oxidation and photoinduced hydrogen evolution.[28,29]

Doping bismuth ion into TiO_2 was studied in the relationship between crystal structure and photocatalytic activity.[24–31] For the Bi–TiO_2 nanofibers synthesized by a hydrothermal method, a small part of Bi transformed to Bi_2O_3 when the doping concentration reached 10.00 mol %.[24] The Bi–TiO_2 nanotubes synthesized by sol–gel method appears rutile TiO_2 phase, and it can enhance the photocatalytic activity.[29] In addition, the Bi–TiO_2 hollow thin sheets prepared by the hydrothermal synthesis also detected a small amount of Bi_2O_3 phase, and it significantly enhanced the photocatalytic performance under visible light irradiation.[31] In summary of these studies, bismuth doping plays an important role in improving the photocatalytic activity and electro-optical characteristics. However, the bismuth doping effect on the crystal structure of Bi–TiO_2 is rarely studied. Hence, our study focus on the correlation between the crystal structure and bismuth doping concentration at various calcination temperatures.

In our study, various Bi–TiO_2 NPs were synthesized by sol–gel method followed by thermal treatment. Bi–TiO_2 NPs were investigated systematically by X-ray diffraction (XRD) to realize the correlation between bismuth doping concentration and its corresponding crystal structure at elevated calcination temperature. A phase diagram for Bi–TiO_2 NPs in doping concentration versus calcination temperature is illustrated to know the applicable window. It is useful for further study in the crystal structure and photocatalytic applications.

2. Experimental procedure

Various bismuth doped titanium oxide gels were prepared by sol–gel method using 36.00 ml titanium isopropoxide [$Ti(OCH(CH_3)_2)_4$, Sigma-Aldrich, 97%] with several amounts of bismuth nitrate (Acros Organics, 99.999%) as the precursor and 107.50 ml 2-propanol (C_3H_7OH, Acros Organics, reagent grade) as the solvent. Aiming to control the pH level, 5.00 ml hydrochloric acid (Acros Organics, 37%) was added to the solution. After that, 1.00 ml deionized water was added to the well mixed solution. The solution was then kept at room temperature to be a gel. After gelation, titanium oxide gel was first calcined under 200 °C to reduce organic compound. Then, the powder was kept calcined under 450, 500, 550, 600, 650, and 700 °C, for 4 h, and its heating rate is 5 °C/min.

For Raman scattering measurements of various Bi–TiO_2 NPs, the samples were placed on a piezoelectric stage of

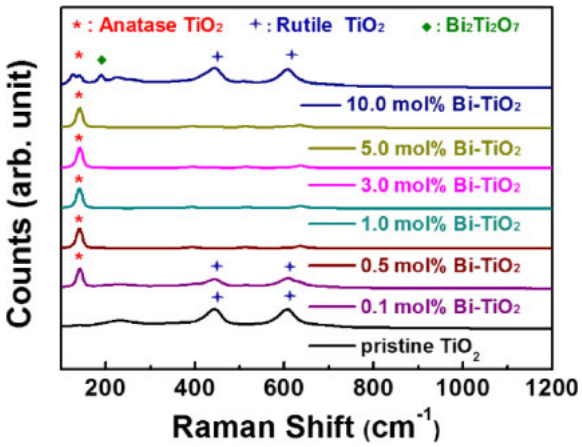

Fig. 1. (Color online) Raman spectra of pristine TiO_2 and various Bi–TiO_2 with different doping concentrations calcined at 650 °C.

Raman spectrometer (UniRAM UniDron) and were excited by a 50 mW 532 nm selective laser melting (SLM) continuous-wave (CW) diode-pumped solid state (DPSS) laser. The laser beam was focused with a 50X objective lens (Nikon plane objective, NA ≈ 0.55, WD ~ 8.2 mm). The diameter of the focused laser beam was about 10 μm. To observe the crystal structure, X-ray diffractometer (Bruker D2 phaser with Xflash 430) was used. UV–vis reflectance spectra of various Bi–TiO_2 samples were measured by UV–vis spectroscopy (Jasco V-630) in the 300–900 nm wavelength range.

To observe the photocatalytic activity, the Bi–TiO_2 NPs were tested by the degradation of methyl orange (Acros Organics, pure). In the experiment, 20.0 mg of catalyst was sonicated for 10 min in 150 mL of 1.0 mg/L methyl orange aqueous solution. The mixture was kept at room temperature. The suspension was irradiated with UV lamps (Sankyo Denki F8T5BL UV-A lamp, the wavelength of maximum emission was at ~352 nm and the power was ~8 W) under vigorous stirring and ambient conditions. For UV source, two lamps were placed above the reactor. The distance between lamp and reactor is about 10.0 cm. Before the actual photodegradation experiments, the suspensions were left to relax for 10 min in order to minimize the error of the dye concentration measurements caused by initial surface adsorption. After centrifuging for 15 min at 5000 rpm, the absorption spectrum of the retained methyl orange and its derivatives in the supernatant was recorded by absorption spectrophotometer (Jasco V-630) in the 300–900 nm wavelength range.

3. Results and discussion

Bi–TiO_2 NPs calcined at 650 °C were analyzed by Raman spectroscopy to observe the vibrational information that is specific to the chemical bonds and symmetry of molecules (Fig. 1). Raman spectrum of pristine TiO_2 shows that it merely has single rutile phase. While bismuth doping concentration increases, rutile phase will transform into anatase phase. As the doping concentration up to 10 mol % at calcination temperature of 650 °C, the bismuth dopant leads to form the multiple phases consisted of bismuth titanate ($Bi_2Ti_2O_7$), rutile TiO_2 and anatase TiO_2.

The crystal structures of Bi–TiO_2 NPs calcined at 650 °C were characterized by XRD, and their XRD patterns are shown in Fig. 2(a). When the calcination temperature is at 650 °C, the pristine TiO_2 NPs is individual rutile phase. Once bismuth was doped to TiO_2, the intensity of anatase TiO_2 phase increased while the rutile phase decreased and finally

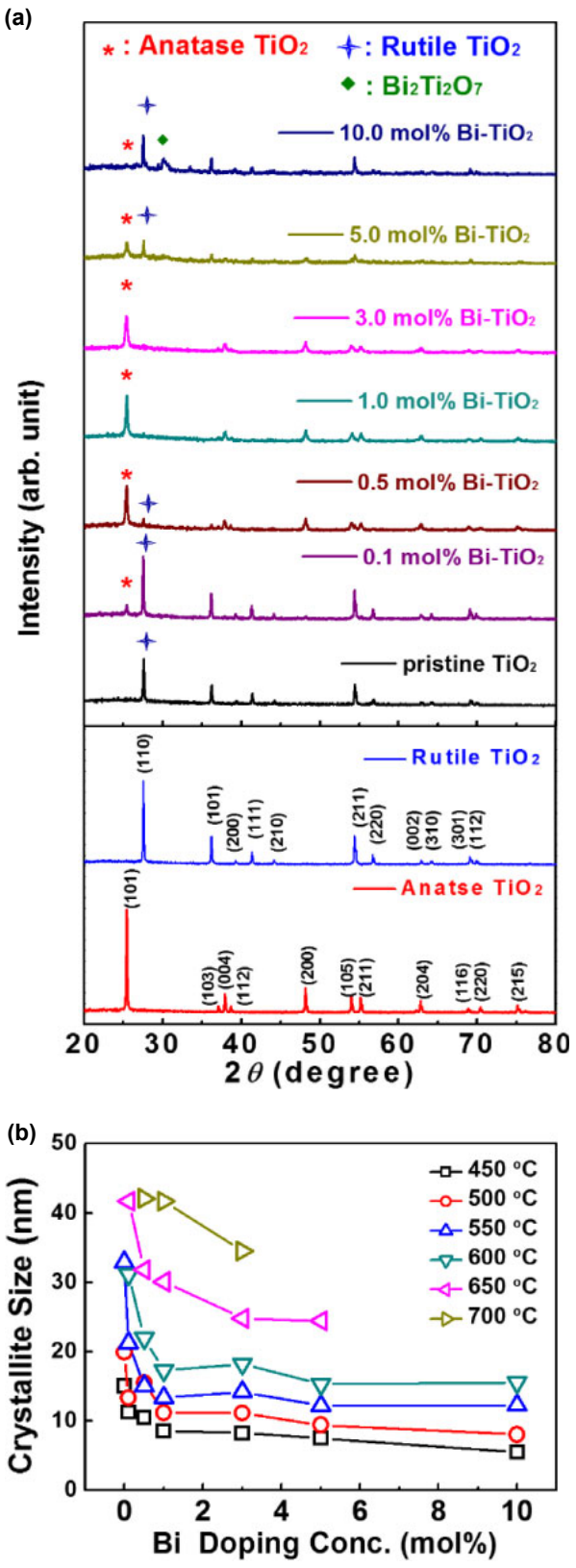

Fig. 2. (Color online) (a) XRD patterns of pristine TiO_2 and various Bi–TiO_2 with various doping concentrations calcined at 650 °C. (b) Estimated crystallite size for (101) plane of anatase TiO_2 phase.

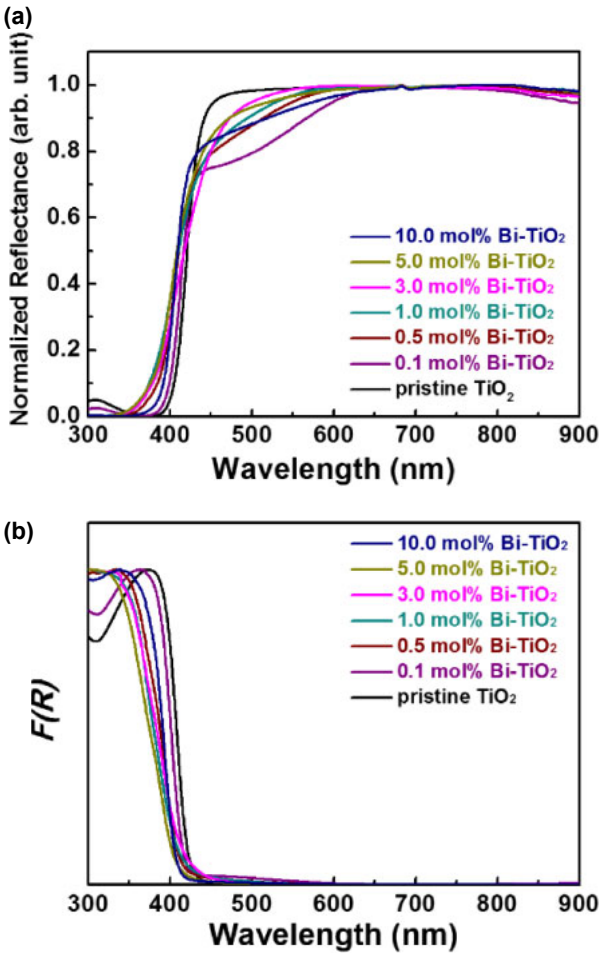

Fig. 3. (Color online) (a) Reflection spectra of pristine TiO_2 and various Bi–TiO_2 with several doping concentration calcined at 650 °C. (b) Kubelka–Munk function of pristine TiO_2 and various Bi–TiO_2.

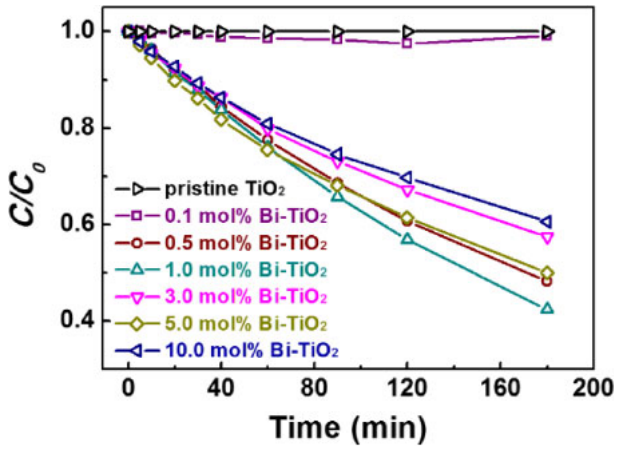

Fig. 4. (Color online) Activities of the pristine TiO_2 and various Bi–TiO_2 with various doping concentrations calcined at 650 °C over the photodegradation of methyl orange under UV irradiation.

disappeared. However, the rutile TiO_2 phase is restrained until the Bi doping concentration is higher than 10.0 mol %. High concentration bismuth doping causes the formation of mixed phase, including $Bi_2Ti_2O_7$,[32–34] rutile TiO_2 and anatase TiO_2. Aiming to discover the bismuth doping effect for crystal structure, we predict the crystallite size of (101) plane in anatase TiO_2 phase by using Debye–Scherrer equation as shown in Fig. 2(b).[35] In addition, the crystallite size of (101) plane in anatase TiO_2 phase were calculated using the XRD patterns of various Bi–TiO_2 NPs calcined at different temperatures (Fig. S1 in the online supplementary data at http://stacks.iop.org/JJAP/56/04CJ01/mmedia). For high temperature calcination process, it leads to the formation of large particles. However, the crystallite size becomes dramatically smaller, and it becomes stable after the doping concentration larger than 3.0 mol %.

The reflection spectra of various Bi–TiO_2 NPs show significantly blue-shift [Fig. 3(a)]. The Kubelka–Munk function, $F(R)$, gives the optical absorbance of various Bi–TiO_2 to be approximated from its reflectance.

$$F(R) = \frac{(1-R)^2}{2R} = \frac{k}{s} = \frac{Ac}{s}$$

Here, R is the reflectance, k is the absorption coefficient, s is the scattering coefficient, c is the concentration of the absorbing species, and A is the absorbance.[36] The relationship between the concentrations and the reflectance of various Bi–TiO_2 is shown in Fig. 3(b). Rutile TiO_2 possesses high absorption and its band gap is about 3.0 eV which is narrower than 3.2 eV of anatase TiO_2.[37] From Fig. 3, the reflectance change is on account of the varying of crystal structures including anatase, rutile and $Bi_2Ti_2O_7$ in several doping concentrations.

Aiming to observe the photocatalytic performance, Bi–TiO_2 NPs with different doping concentration were tested to find the highest photocatalytic activity under UV irradiation. For the photocatalytic activity of various Bi–TiO_2 NPs, the absorption spectra of methyl orange as a function of UV irradiation time were recorded. The absorbance at $\lambda = 464$ nm was used to calculate the methyl orange concentration by a calibration curve measured previously. The color of suspension is changed from the initial orange color to colorless. The C/C_0 curve, where C_0 is the initial concentration and C is the concentration of the dye at testing time t, the photodegradation percentages of methyl orange at different time are shown in Fig. 4. The photodegradation test indicated that 1.0 mol % Bi–TiO_2 has the highest degradation performance. High bismuth concentration doping resulted in the destruction of crystal structure, which impeded the electron/hole transport for the 10.0 mol % Bi–TiO_2.

In order to find out the bismuth doping effect on crystal structure, we synthesized a series of Bi–TiO_2 with different doping concentration calcined at various temperatures for further study. For the bulk TiO_2 materials, the temperature of anatase–rutile phase transition is ~600 °C.[38,39] However, the anatase–rutile phase transition temperature of the synthesized TiO_2 nanoparticles in our study is only ~550 °C. When the material dimension decreases towards the nanoscale, the crystal structure transition temperature could also reduce with decreasing the material dimension. For the Bi_2O_3–TiO_2 system studied by Kargin group,[40] they reported that $Bi_2Ti_2O_7$ decomposes to $Bi_2Ti_4O_{11}$ and $Bi_4Ti_3O_{11}$ during 700–1000 °C. Once the temperature is above 1000 °C, $Bi_2Ti_2O_7$ will appear again. In our study, the phase diagram of Bi–TiO_2 was draw according to the XRD data as shown in Fig. 5. Under the calcination temperature of 500 °C, all Bi–TiO_2 NPs are still anatase TiO_2 phase even the doping concentration is as high as 10.0 mol %. When the calcination

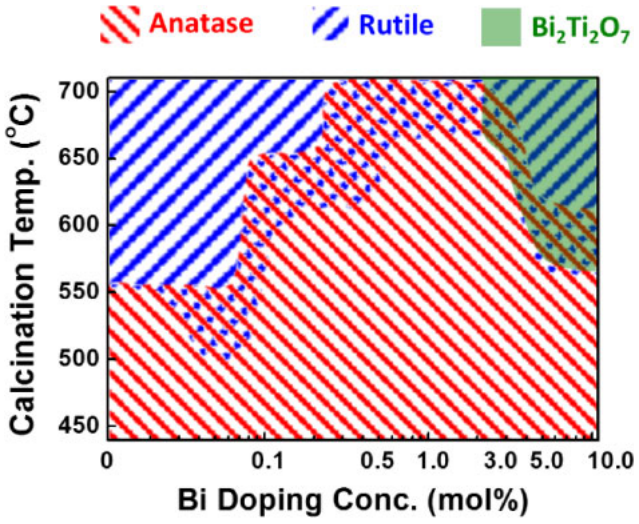

Fig. 5. (Color online) Phase diagram of TiO_2 doped with different bismuth concentrations and calcination temperatures.

temperature is above 550 °C, the crystal structure changes from anatase to rutile for low doping concentration Bi–TiO_2 NPs (<0.1 mol % doping concentration). Moreover, with the increasing of bismuth doping concentration, the anatase TiO_2 phase will appear again and finally decrease at high doping concentration. Once the anatase TiO_2 decreases, bismuth titanium ($Bi_2Ti_2O_7$) and rutile TiO_2 will appear at higher doping concentration (>5.0 mol %) and higher calcination temperature (>600 °C). Hence, bismuth doping concentration and calcination temperature will affect the formation of multiple phases for Bi–TiO_2, including anatase TiO_2, rutile TiO_2 and $Bi_2Ti_2O_7$.

4. Conclusions

We developed a series of Bi–TiO_2 NPs successfully and studied their crystal structure and photocatalytic activity. The photocatalytic activity can be easily modified by varying the bismuth doping concentration. By combining the XRD diffraction analysis, a simple phase diagram for various Bi–TiO_2 NPs in doping concentration versus calcination temperature is provided. It can be useful for further study in crystal structure and related photocatalytic applications.

Acknowledgements

The authors appreciate Mr. Shih-Han Huang and Mr. Yu-Kai Tseng for the preparation of Bi–TiO_2 NPs and Dr. Ming-Tao Lee group (BL-13A1) at National Synchrotron Radiation Research Center for useful discussion. The authors wish to acknowledge the financial support of Ministry of Science and Technology of Taiwan (MOST 105-2221-E-182-011, MOST 105-2632-E-182-001, and MOST 105-3113-E-002-010) and Chang Gung Memorial Hospital, Linkou (CMRPD2F0161, CMRPD2E0072, and BMRPC74).

1) D. Bahnemann, Sol. Energy **77**, 445 (2004).
2) D. Chatterjee and S. Dasgupta, J. Photochem. Photobiol. C **6**, 186 (2005).
3) K. Ohkawa, W. Ohara, D. Uchida, and M. Deura, Jpn. J. Appl. Phys. **52**, 08JH04 (2013).
4) S. Kogoshi, S. Araki, S. Yazawa, T. Nakano, T. Takeuchi, N. Katayama, Y. Kudo, and T. Nakanishi, Jpn. J. Appl. Phys. **53**, 098001 (2014).
5) A. Fujishima and K. Honda, Nature **238**, 37 (1972).
6) P. K. Song, Y. Irie, Y. Sato, and Y. Shigesato, Jpn. J. Appl. Phys. **43**, L358 (2004).
7) M. Zimmermann and G. Garnweitner, CrystEngComm **14**, 8562 (2012).
8) S. B. Rawal, S. Bera, D. Lee, D.-J. Jang, and W. I. Lee, Catal. Sci. Technol. **3**, 1822 (2013).
9) M. Zhang, J. Hou, J. Wu, and J. Yang, Jpn. J. Appl. Phys. **53**, 115505 (2014).
10) A. Kudo and Y. Miseki, Chem. Soc. Rev. **38**, 253 (2009).
11) J.-Y. Liao, J.-W. He, H. Xu, D.-B. Kuang, and C.-Y. Su, J. Mater. Chem. **22**, 7910 (2012).
12) T. Ochiai, T. Hoshi, H. Slimen, K. Nakata, T. Murakami, H. Tatejima, Y. Koide, A. Houas, T. Horie, Y. Morito, and A. Fujishima, Catal. Sci. Technol. **1**, 1324 (2011).
13) U. Shaislamov and B. L. Yang, Int. J. Hydrogen Energy **38**, 14180 (2013).
14) H. Sheng, Q. Li, W. Ma, H. Ji, C. Chen, and J. Zhao, Appl. Catal. B **138–139**, 212 (2013).
15) X. Sun, Q. Sun, Y. Li, L. Sui, and L. Dong, Phys. Chem. Chem. Phys. **15**, 18716 (2013).
16) M. Ozawa, H. Matui, and S. Suzuki, Jpn. J. Appl. Phys. **55**, 01AG04 (2016).
17) R. G. F. Costa, C. Ribeiro, and L. H. C. Mattoso, J. Appl. Polym. Sci. **127**, 4463 (2013).
18) T. Shibata, H. Irie, M. Ohmori, A. Nakajima, T. Watanabe, and K. Hashimoto, Phys. Chem. Chem. Phys. **6**, 1359 (2004).
19) Z. Zhu and R.-J. Wu, J. Taiwan Inst. Chem. Eng. **50**, 276 (2015).
20) M. Ni, M. K. H. Leung, D. Y. C. Leung, and K. Sumathy, Renewable Sustainable Energy Rev. **11**, 401 (2007).
21) T. Morikawa, R. Asahi, T. Ohwaki, K. Aoki, and Y. Taga, Jpn. J. Appl. Phys. **40**, L561 (2001).
22) M.-C. Wu, J. Hiltunen, A. Sápi, A. Avila, W. Larsson, H.-C. Liao, M. Huuhtanen, G. Tóth, A. Shchukarev, N. Laufer, Á. Kukovecz, Z. Kónya, J.-P. Mikkola, R. Keiski, W.-F. Su, Y.-F. Chen, H. Jantunen, P. M. Ajayan, R. Vajtai, and K. Kordás, ACS Nano **5**, 5025 (2011).
23) W. Avansi, R. Arenal, V. R. de Mendonca, C. Ribeiro, and E. Longo, CrystEngComm **16**, 5021 (2014).
24) M.-C. Wu, J.-S. Chih, and W.-K. Huang, CrystEngComm **16**, 10692 (2014).
25) M. Asemi and M. Ghanaatshoar, Appl. Phys. A **122**, 853 (2016).
26) M.-C. Wu, W.-C. Chen, T.-H. Lin, K.-C. Hsiao, K.-M. Lee, and C.-G. Wu, Sol. Energy **135**, 22 (2016).
27) J. H. Lee, H. Lee, and M. Kang, Mater. Lett. **178**, 316 (2016).
28) Y. Chen, D. Chen, J. Chen, Q. Lu, M. Zhang, B. Liu, Q. Wang, and Z. Wang, J. Alloys Compd. **651**, 114 (2015).
29) T. S. Natarajan, K. Natarajan, H. C. Bajaj, and R. J. Tayade, J. Nanopart. Res. **15**, 1669 (2013).
30) Y. Wu, G. Lu, and S. Li, J. Phys. Chem. C **113**, 9950 (2009).
31) W. Wang, D. Zhu, Z. Shen, J. Peng, J. Luo, and X. Liu, Ind. Eng. Chem. Res. **55**, 6373 (2016).
32) W. F. Yao, H. Wang, X. H. Xu, J. T. Zhou, X. N. Yang, Y. Zhang, and S. X. Shang, Appl. Catal. A **259**, 29 (2004).
33) Y. Zhang, Y. Zhang, B. Fu, M. Hong, and M. Xiang, Ceram. Int. **41**, 10243 (2015).
34) W. S. Al-Arjan, M. M. F. Algaradah, J. Brewer, and A. L. Hector, Mater. Res. Bull. **74**, 234 (2016).
35) A. L. Patterson, Phys. Rev. **56**, 978 (1939).
36) V. Barron and J. Torrent, Eur. J. Soil Sci. **37**, 499 (1986).
37) L. G. Devi and R. Kavitha, Appl. Catal. B **140–141**, 559 (2013).
38) J. C. Jamieson and B. Olinger, Am. Mineral. **54**, 1477 (1969).
39) D. A. H. Hanaor and C. C. Sorrell, J. Mater. Sci. **46**, 855 (2011).
40) Y. F. Kargin, S. N. Ivicheva, and V. V. Volkov, Russ. J. Inorg. Chem. **60**, 619 (2015).